

APR 1

0154

1. REPORT DATE (DD-MM-YYYY)

02-04-2002

## 2. REPORT TYPE

## Final

3. DATES COVERED (From - To)

01 Feb 99 – 30 Nov 01

4. TITLE AND SUBTITLE

## TECHSAT21-PULSED ELECTRIC MICROTHRUSTERS WITH SOLID PROPELLANT FOR MICROSATS AND NANOSATS

5a. CONTRACT NUMBER

5b. GRANT NUMBER

F49620-99-1-0123

5c. PROGRAM ELEMENT NUMBER

6. AUTHOR(S)

Rodney L. Burton

5d. PROJECT NUMBER

5e. TASK NUMBER

2305/CV

5f. WORK UNIT NUMBER

7. PERFORMING ORGANIZATION NAME(S) AND ADDRESS(ES)

Aeronautical & Astronautical Engineering  
306 Talbot, 104 S. Wright St.  
Urbana, IL 61801

## 8. PERFORMING ORGANIZATION REPORT

9. SPONSORING / MONITORING AGENCY NAME(S) AND ADDRESS(ES)

Air Force Office of Scientific Research  
801 N. Randolph St Room 732  
Arlington, VA 22203-1977

10. SPONSOR/MONITOR'S ACRONYM(S)  
AFOSR/NA

11 SPONSOR/MONITOR'S REPORT  
NUMBER(S)

## 12. DISTRIBUTION / AVAILABILITY STATEMENT

11. APPROVED FOR RELEASE BY THE DIRECTOR, ARPA, ON 08-09-2013

### 13. SUPPLEMENTARY NOTES

## 14. ABSTRACT

This report describes progress, in experimental development, plasma diagnostics, and modeling, in advanced pulsed plasma thrusters (PPT) for application to formation-flying satellite constellations such as TechSat21. The research concentrated on coaxial Teflon PPTs, predominantly of the electrothermal (high thrust) type, with an average power of 100 watts. During this effort, performance advances were made both in the thruster design and in the pulsed circuitry driving the discharge, aided by increased understanding derived from a two-fluid model. The results of this research led to the development, under separate contract to CU Aerospace, of a PPT flight test model (PPT-8) which was tested at the AFRL Electric Propulsion Laboratory.

## 15. SUBJECT TERMS

Electric propulsion, Pulsed thruster, Teflon.

16. SECURITY CLASSIFICATION OF: Unclassified

## 17. LIMITATION OF ABSTRACT

18. NUMBER OF PAGES

**19a. NAME OF RESPONSIBLE PERSON** Rodney L. Burton

### a. REPORT

b. ABSTRACT

c. THIS PAGE

19b. TELEPHONE NUMBER (include area code)

217-244-6223

Standard Form 298 (Rev. 8-98)  
Prescribed by ANSI Std. Z39.18

20020509 010

# **FINAL REPORT**

**(Period from 1 February, 1999 to 30 November, 2001)**

**Pulsed Electric Microthrusters with  
Solid Propellant for Microsats and Nanosats**

**Rodney L. Burton, Principal Investigator**

**University of Illinois at Urbana-Champaign**

**Department of Aeronautical and Astronautical Engineering  
104 S. Wright Street  
Urbana, IL 61801**

**R. L. Burton  
217-244-6223  
217-244-0720  
rburton@uiuc.edu**

**GRANT NUMBER: F49620-99-1-0123**

**Start date of Grant: 2/01/99**

**End Date of Grant: 11/30/2001**

# Pulsed Plasma Thruster Final Report

## ABSTRACT

This report describes progress, in experimental development, plasma diagnostics, and modeling, in advanced pulsed plasma thrusters (PPT) for application to formation-flying satellite constellations. The research concentrated on coaxial Teflon PPTs, predominantly of the electrothermal (high thrust) type, with an average power of 100 watts. During this effort, performance advances were made both in the thruster design and in the pulsed circuitry driving the discharge, aided by increased understanding derived from a two-fluid model. The results of this research led to the development, under separate contract to CU Aerospace, of a PPT flight test model (PPT-8) which was tested at the AFRL Electric Propulsion Laboratory.

Experiments are performed on a cylindrically-symmetric Teflon electrothermal thruster with variable geometry, energy and pulse rate. Measurements are made of pulse energy and current, mass loss, impulse bit, and heat loss. The results show that the specific mass loss is linear with cavity length, and roughly independent of energy. The specific thrust is roughly constant with energy ( $> 35 \text{ N-s/J}$ ) for high energies, but decreases somewhat for low energies. The highest specific impulse is achieved with the shortest cavity length. Comparison with a two-stream model suggests that the fraction of late-time ablation is on the order of 10%, compared to 40% for the LES-8/9 thruster, and that a rarefaction wave model can be used to predict the impulse bit with an empirically-determined proportionality constant. Heat loss measurements as a function of discharge energy show a larger fraction of heat loss for lower energy, consistent with the observed reduced performance at that condition.

Diagnostics are performed using a Herriott Cell to increase the optical path length. Traditional interferometric techniques have been shown to lack the resolution needed to characterize the electron and neutral densities in the diffuse plasma of the Pulsed Plasma Thruster (PPT) exhaust. In the present work, a Herriott cell is added into a standard quadrature heterodyne interferometer to increase sensitivity for electron density measurements, and allow measurements of neutral densities amidst mechanical vibration. Measurements of electron and neutral density during and after the current pulse are sought for the purposes of modeling spacecraft contamination from PPTs. Testing is performed on the UIUC PPT-4, a coaxial electrothermal PPT pulsing at 20 J. Analytical and experimental analysis are conducted to determine the integrity of the phase front and the effect of multiple passes on the density measurements taken. Up to 18-passes through the plasma are accomplished using the Herriott cell, while maintaining sufficient phase-front quality for interferometric analysis. The advantage of the cell is obvious at late times when the external mechanical vibrations induce an apparent phase shift in the same direction as for neutral particles. Due to the same dependence on wavelength, 2 laser frequencies cannot be used to separate neutral and mechanical vibration contributions. The Herriott cell allows a density resolution increase linear with the number of passes that does not increase the mechanical vibrational component. Uncertainties from both mechanical vibrational sources and shot-to-shot variations of the thruster itself are investigated and characterized for this system. Due to variations in mechanical vibrations on a day to day basis, the cell is able to characterize the neutral density of the thruster only over short time periods. At 200  $\mu\text{s}$  for single tests ( $\sim 20$  shots averaged) at 14 and 18 passes neutral density at the exit plane was shown to be no more than  $1 \times 10^{16} \text{ cm}^{-3}$ . Average peak electron density (4  $\mu\text{s}$ )

was shown to be  $5.0 \pm 1.1 \cdot 10^{15} \text{ cm}^{-3}$ , however the single shot error due to the Herriott cell is  $\pm 10^{12} \text{ cm}^{-3}$ .

Finally, we have developed a new theory of PPT operation called the Two-Stream Model, which has led to increased understanding of PPT operation, greatly increased performance, and shows the way to a new class of high- $I_{sp}$  PPTs with much higher efficiency. The theory assumes that the exhaust stream is split into two co-flowing streams, one fast and one slow, which average together to give the measured thrust and specific impulse. A key hypothesis, justified from the work of Alfven and related experiments on partially ionized plasmas, is that the velocity difference of the two streams is equal to the Alfven critical velocity.

## I. Experimental Effort – Effects of Geometry and Energy on a Coaxial Teflon PPT

### Introduction

The pulsed plasma thruster is a robust, solid state device that has flown on a number of missions.<sup>1</sup> The PPT uses a high current, few microsecond pulse to evaporate, ionize, and accelerate a solid fuel to produce thrust. The power input can be throttled by varying either the energy of each pulse, or the pulse rate, making it a versatile thruster capable of performing both attitude control missions as well as orbit raising. Since the fuel is inert and solid, usually Teflon, PPT fuel feed mechanisms are neither complicated nor are they hazardous. PPTs have higher  $I_{sp}$  than chemical thrusters, which allows a higher payload mass.

There are two types of acceleration mechanisms employed in a PPT. Electromagnetic acceleration produces thrust by accelerating ionized particles using the self-induced magnetic field. Electromagnetic PPTs are often characterized by a high  $I_{sp}$  and lower thrust. Electrothermal acceleration uses the pressure generated by the discharge to accelerate particles. In a coaxial PPT, the arc ablates the propellant from the walls of a central chamber, increasing the chamber pressure. Particles are then accelerated in an unsteady manner by the pressure gradient through a nozzle.

### Experiments

A series of experiments were performed to help determine the effects of geometry and energy on the performance of an electrothermal thruster (PPT-7). The thruster (Figs 1 and 2) is coaxial, using tubular Teflon propellant. The tube is clamped inside a Teflon bracket, which also supports the central brass electrode. The other end of the cavity connects to a boron nitride nozzle with a 25° half angle. An integral semiconductor type spark plug,<sup>2</sup> used to initiate the discharge, is mounted in the nozzle. The 29 mm diameter cathode is at the exit of the nozzle.

Tests with stored energy less than 50 J use 14 parallel mica capacitor sections,<sup>2</sup> with a total capacitance of 9.2  $\mu\text{F}$ . In order to test at 70 J, 7 more sections are added, increasing the capacitance to 14.1  $\mu\text{F}$ . The 50 J baseline current and capacitor voltage pulse is underdamped (Fig. 3), and displays a peak current of 27 kA at 160 kHz.

A number of diagnostics were used during these tests. The UIUC compact thrust stand<sup>3</sup> was used in single pulse mode to measure the thrust. At least 10 thrust measurements were taken for each geometry tested. The current was recorded using a Rogowski coil on the central electrode and a 1000:1 high voltage probe (Tektronix P6015) was used to measure the capacitor discharge voltage at the vacuum tank feedthrough. Temperature measurements of the propellant and one capacitor pack were taken using type K thermocouples. The mass of the fuel was recorded to within 0.1 mg before and after each 2000 pulse test.

The thruster surface temperature measurement was used to determine the heat loss from the thruster. Starting from room temperature at constant pulse rate, the temperature is observed, after an initial transient phase, to rise linearly at the outer surface. The heating of the component is determined from the measured constant temperature rise rate and the thermal mass ( $mC_p$ ), according to

$$\dot{Q} = G(mC_p)\dot{T} \quad (1)$$

where the factor  $G$  is 1.0 for the capacitor and is  $\sim 2.3$  to account for the radial temperature gradient in the thruster. Typically, the temperature rise rate was  $15^{\circ}\text{C}$  in 10 minutes. The thermal mass of the capacitors was determined calorimetrically, using a dewar, by submerging a capacitor section in an equal mass of warm water. The thruster thermal mass was determined by calculating the sum of the masses and specific heats of the thruster components in close mechanical contact to the discharge chamber.

**Table 1. Thermal masses used in heat loss calculations**

Item	Mass [g]	$mC_p$ [J/ $^{\circ}\text{C}$ ]
9.2 $\mu\text{F}$ Capacitor	2390	1780
14.1 $\mu\text{F}$ Capacitor	3520	2630
Thruster	350	310

The heating rates calculated by this technique are in error because of the heat flow from the thruster to the capacitor through the transmission line, estimated to be less than 1 W.

Each geometry tested is characterized by the cavity diameter near the rear electrode, the cavity length, and the cavity exit diameter. The baseline constant diameter geometry for these experiments is 14/35/14, denoting a 14 mm rear cavity diameter, 35 mm length, and a 14 mm front cavity diameter. From this baseline case, three other diameters and two other lengths were tested. Tests also were performed without a nozzle in order to determine its effect on performance. Two lengths of tapered cavities were also tested: 3.5/20/14 and 3.5/35/14 with  $15^{\circ}$  and  $10^{\circ}$  half angle respectively. These options are illustrated in Table 2. The baseline energy is 50 J, with 5 other energies tested. In order to help illustrate the difference in heat loss at different energies, a test was run at the same power as the baseline, but a different energy.

A test was performed to help illustrate the effect that the nozzle has on performance. In order to protect the nylon spark plug mount and the bulkhead from the plasma, a polyethylene insert was used to replace the nozzle. The insert has an exit diameter of 29 mm and is the same length at the nozzle, 17.3 mm. During these tests, 0.7 % of the mass ablated was from the polyethylene insert, which is not enough to affect the performance of the thruster.

**Table 2. List of parameters varied from baseline**

Parameter	Values
Diameter	8,11,14,17 [mm]
Length	20,35,50 [mm]
Energy	10,12.5 J (4 Hz),15,20,28, 50,70 [J]
Pulse Rate	1 Hz, 4 Hz
Taper	$10^{\circ}$ half angle, $15^{\circ}$ half angle
Nozzle	With nozzle, Without Nozzle

## **Test procedure**

Each test consisted of 1000 shots repetitive firing at 1 Hz to warm up the thruster and burn-in the fuel tube. After burn-in, 10 thrust measurements were taken in single pulse mode, followed by another 1000 shots to reduce error in the mass loss measurement. Each pulse produces a thrust stand position transducer (LVDT) output which is a slowly decaying sinusoid. The initial ( $t = 0$ ) slope is determined by curve-fitting an analytical damped sinusoid to the LVDT waveform, which gives the post-pulse thrust stand platform velocity  $u_p$ . The impulse bit is  $u_p$  multiplied by the platform mass, which is weighed for each test setup. Thermocouple data, including the capacitor and fuel temperature, were recorded during all repetitive pulsing phases of the test.

## **Results**

The following plots represent the data taken. Figures 4 - 6 show the  $I_{sp}$ , specific thrust, and specific mass loss versus energy respectively. Figures 7 - 9 show the same performance parameters plotted versus cavity length. Figures 10 - 12 are plots of the same parameters, but plotted versus cavity diameter. These plots have data points representing the no-nozzle case, and the tapered cavity cases.

There are several sources of experimental error. From test to test, the impulse bit measurement standard deviation is 3% at high energy and 6% at lower energy. Some of this may be attributed to shot-to-shot thrust variation, but a larger portion of this is due to LVDT noise. Error due to the curve-fit is  $< 0.5\%$ . Sufficient thrust measurements were taken for each test to provide a statistically valid sample. The mass of the thrust stand platform is known to within 0.5%. The error in the energy measurement is approximately 0.5%. The total uncertainty at high energy for the measurements taken is 3%.

## **Analysis – Discussion**

**Mass loss.** The pulse specific mass loss ( $\mu\text{g/J}$ ) is relatively constant with energy for the baseline (14/35/14) geometry. With diameter, specific mass loss is seen to increase for decreasing diameters, presumably because of the higher current density and temperature. The specific mass loss is approximately proportional to length, as reported previously.<sup>4,5,6</sup>

**Specific Thrust.** The specific thrust is relatively constant with energy at  $35 \mu\text{N-s/J}$  from 20 – 70 J, and then decreases at lower energies. This behavior is consistent with a heat loss model of  $\Delta Q_{\text{loss}} = A + BE$ , where A and B are constants and E is the discharge energy. Heat loss measurements as a function of energy are given below. With diameter, specific thrust increases monotonically with decreasing diameter, possibly due to lower heat loss with reduced Teflon surface area exposed to the discharge. The specific thrust is linear with length at 50 J, approximately equal to  $17 + 11 L_{\text{mm}}$  ( $\mu\text{N-s/J}$ ).

**Specific Impulse.** Specific impulse generally increases with energy, from 330 s at 10 J to 490 s at 70 J (baseline geometry). With diameter,  $I_{sp}$  reaches a maximum of 450 s at 14 mm (baseline).  $I_{sp}$  increases to above 500 s for lengths  $< 25$  mm, and some benefits (610 s) is shown for a short tapered cavity.

Although most of the thrust is produced by electrothermal acceleration, there is a small fraction produced by electromagnetic acceleration. The amount of impulse per joule (impulse bit) produced electromagnetically is:<sup>7</sup>



$$\int T dt = \frac{\mu_o \Psi}{4\pi} \left[ \ln \left( \frac{r_a}{r_c} \right) + \frac{1}{2} \right] \quad (2)$$

where  $\Psi = \int I^2 dt$ ,  $r_a$  and  $r_c$  are the annular and central electrode radii respectively, and  $\mu_o$  is the magnetic permeability of free space. With a typical  $\Psi = 1600 \text{ A}^2\text{-s}$ , the force due to the electromagnetic contribution is approximately  $200 \mu\text{N-s}$ . The percentage of impulse bit that is electromagnetic is then  $\beta = 0.11$ .

The thruster efficiency  $\eta_t$  can be expressed as the product of component sub-efficiencies.<sup>7</sup> These efficiencies include the pulse energy transfer  $\eta_{tr}$ , thruster heat loss  $\eta_h$ , frozen flow  $\eta_f$ , exhaust beam divergence  $\eta_{div}$ , and exhaust velocity distribution efficiency  $\eta_{dist}$ .

$$\eta_t = \eta_{tr} \times \eta_h \times \eta_{ff} \times \eta_{div} \times \eta_{dist} \quad (3)$$

The transfer efficiency takes into account the energy lost to the equivalent series resistance (ESR) of the capacitor. This energy is estimated from the temperature increase during a 50 W test, and the thermal mass of the capacitor. For the baseline case,  $Q = 3.7 \text{ W}$ . Approximately 1 W of this is due to heat transfer from the thruster, leaving 2.7 W of internal heating. This is 5.4% of the 50 W making the  $\eta_{tr} = .95$ . Another way to estimate the energy lost to the capacitor is from the relation capacitor heating/pulse =  $\Psi \times \text{ESR}$ . A separately-measured capacitor ESR of  $2.8 \text{ m}\Omega$  for the baseline case,<sup>2</sup> gives 4.5 W, making  $\eta_{tr} = .91$ . We adopt a value of  $\eta_{tr} = 0.93$ .

The thruster heat loss efficiency is measured from the temperature rise above room temperature for a given time interval. Since heat distributes itself slowly throughout the entire thruster, only the parts of the thruster in mechanical contact with the fuel were used to determine a thermal mass ( $310 \text{ J/}^\circ\text{C}$ ). A calculated correction factor ( $G \sim 2.3$ ) is used to take into account the higher temperature rise rate of the thruster mass closer to the discharge than the thermocouple location. Multiplying the temperature rise rate by the thruster thermal mass, and the factor  $G$ , the energy lost to heating the thruster is 13.1 W, resulting in  $\eta_h = .74$ .

**Table 3 Heat loss summary**

	Power [Watts]	Efficiency
Power in	50	
Capacitor	$3.6 \pm 0.9$	$\eta_{tr} = 0.93$
Thruster	13.1	$\eta_h = 0.74$

Combining  $\eta_{tr}$  and  $\eta_h$ ,  $0.93 \times 0.74 = 0.69$  of the stored energy is available for propulsion.

### **Two-Stream Model**

We now determine the rest of the component efficiencies by employing a two-stream model<sup>7</sup> for the exhaust of the PPT. In the two-stream model, the exhaust of a PPT is comprised of fast particles (ions) accelerated electromagnetically, slow particles (neutrals) accelerated electrothermally, and particles ablated late in the pulse with virtually no velocity. The relative velocity between the ions and neutrals is limited by the Alfven critical velocity  $u_c$ . For Teflon,  $u_c$



= 13.3 km/s.<sup>7</sup> Both the velocity distribution efficiency and the frozen flow efficiency can be obtained from the two-stream model and experimental data.<sup>1</sup>

The frozen flow efficiency is a measure of the fraction of energy that is converted to kinetic energy in the plasma exhaust plume. In the two-stream model, the frozen flow efficiency is the mass averaged frozen flow efficiency of the fast and the slow particles:

$$\eta_f = \alpha\eta_{ff} + (1 + \alpha)\eta_{fs}C_N \quad (4)$$

where  $\alpha$  is the fast particle mass ratio  $m_f/m$ .  $\eta_{ff}$  and  $\eta_{fs}$  are the frozen flow efficiency for the fast and slow particles respectively. For Teflon fuel, it has been empirically determined that  $\eta_{ff} = .68$  and  $\eta_{fs} = .15$  for an assumed temperature of 2 eV.  $C_N$  is a nozzle thrust coefficient. The "no nozzle" test (Fig.11) produced the same impulse bit as the nozzled test. This implies that for this geometry, the nozzle has no appreciable effect on the thrust, resulting in  $C_N = 1$ .

The fast particle mass ratio  $\alpha$  is a function of the late time ablation factor  $\Phi$ , the electromagnetic impulse bit fraction  $\beta$ , exhaust velocity, and  $u_c$ . It has been found that a portion of the exhaust mass is assumed to exit at late times and with virtually no velocity. This mass does not contribute to the thrust, and is simply lost mass. The variable  $\Phi$  in the two-stream model denotes the fraction of the exhaust mass that contributes to the thrust.

The distribution efficiency, which results from expressing thruster efficiency in terms of momentum rather than kinetic energy, becomes in the two-stream model:

$$\eta_{dist} = \left| \frac{\alpha(\Phi - \alpha)}{\Phi\beta^2 + \alpha(1 - 2\beta)} \right| \quad (5)$$

The divergence efficiency is a measure of losses due to plume divergence, and is taken as

$$\eta_{div} = 0.5[1 + \cos(25^\circ)] = 0.95. \quad (6)$$

Figure 13 shows a plot of specific thrust vs.  $I_{sp}$  using the two-stream model for the 14/35/14 geometry with 3 lines of constant  $\Phi$ . The  $\beta$ ,  $\eta_{tr}$  and  $\eta_h$  used on the plot are those calculated for the baseline case. Although some of the points plotted have a different  $\beta$ , they range between 0.09 and 0.12, making the plot a valid representation. Also, the  $\eta_{tr}$  and  $\eta_h$  are expected to be very similar for a given geometry, for energies above 30 J. From the plot one can estimate  $\Phi = 0.9 \pm 0.1$ . With  $\Phi = 0.9$ ,  $\eta_f$ ,  $\eta_{dist}$ , and  $\eta_t$  are calculated from the two-stream model. The following table shows a summary of all the variables described.

**Table 4 Summary of thruster variables**

Variable	
$\Phi$	0.9
$\beta$	0.11
$\alpha$	0.03
$\eta_{tr}$	0.93
$\eta_h$	0.74
$\eta_f$	0.16
$\eta_{dist}$	0.74
$\eta_{div}$	0.95
$\eta_t$ (model)	0.08
$\eta_t$ (experiment)	0.08

Table 4 illustrates the source of the greatest losses based on the two-stream model. It shows that 97% of the particles in the exhaust plume are slow neutrals. This, combined with the fact that slow particles have a frozen flow efficiency  $\eta_{fs} = 0.16$  results in the largest loss in efficiency. This result implies that the most beneficial way to increase efficiency is to increase  $\alpha$  by ionizing a larger fraction of the discharge, and producing a more electromagnetic thrust.

### **Rarefaction Wave Model**

To model the impulse bit, we assume that the energy deposition time is zero, and that the plasma is a uniform column, producing a pressure thrust on the central electrode until reached by a rarefaction wave moving at sound speed traversing the length of the chamber. It is also assumed that all heat loss occurs during energy deposition. With these assumptions, the mass of the plasma in the chamber is  $m_{gas} = \rho AL$ , where  $\rho$  is the density of the plasma,  $A$  is the cross sectional area of the cavity, and  $L$  is the cavity length. With the ideal gas law assumption, the energy stored in the plasma can then be written as:

$$E = \rho A L e = \frac{p A L e}{RT} \quad (7)$$

where  $p$  is the pressure and  $e$  is the internal energy. This can be rearranged to solve for the electrothermal specific thrust:

$$\frac{pAt_p}{E_o} = KC_N(E/E_o) \left( \frac{p}{\rho ea} \right) \quad (8)$$

where  $a$  is the sound speed, the rarefaction wave travel time is  $t_p = L/a$ , and  $E/E_o$  is the fraction of energy not lost to heat ( $\eta_{tr}\eta_h$ ). The nozzle coefficient is  $C_N = 1$  for these experiments. Because some of the assumptions are approximate, a factor  $K$  is introduced to account for the finite time in which the current pulse occurs, as well as for wall drag, axial flow, and plasma cooling during wave travel. In order to determine  $K$ , the thermodynamic properties of the plasma must be known.

The plasma temperature is determined by modeling the plasma as a black body, radiating energy as  $E = t_p \sigma_{SB} T^4 A$  where  $A$  is the surface area of the cavity including the ends. With a pulse length of  $4 \mu s$ ,  $T = 21250 \text{ K}$  ( $1.8 \text{ eV}$ ). The plasma temperature can also be estimated by calculating the plasma resistance as a Spitzer plasma resistance. The total circuit resistance,  $R = E_o/\Psi = 31 \text{ m}\Omega$  is the sum of the resistances due to the plasma, cavity wall loss, sheath, transmission line, and ESR. By estimating these resistances at approximately  $10 \text{ m}\Omega$ ,  $R_{pl} = 21 \text{ m}\Omega$ . By setting that to the Spitzer formulation,<sup>8</sup>  $T = 22600 \text{ K}$  ( $1.9 \text{ eV}$ ).

From above temperature estimates we take  $T = 21900 \text{ K}$ . Using a table of plasma properties,<sup>9</sup> the thermodynamic quantity  $p/\rho ea$  is determined for an assumed  $p = 1 \text{ atm}$ . From Eq. 8 we find  $K = 1.5$ .

Figures 4 - 6 show that the performance is reduced at low energy ( $< 20 \text{ J}$ ). Eq. 8 suggests that the energy factor  $E/E_o = \eta_{tr}\eta_h$  could be a major contributor to this performance drop. This hypothesis was evaluated by a test in which the power to the thruster remained constant at  $50 \text{ W}$ , but the energy of the pulses was  $50 \text{ J}$  and  $12.5 \text{ J}$  at  $1 \text{ Hz}$  and  $4 \text{ Hz}$  pulse rate. The thermal mass and temperature rise rate of the thruster were then used to determine the power lost to heating, as described previously. It was found that in the  $12.5 \text{ J}$  test,  $58\%$  of the power was lost to heating and in the  $50 \text{ J}$  test only  $26\%$  of the power was lost to heating. This clearly demonstrates that the energy lost to heating is greater at the lower energy. Assuming  $\eta_{tr} = 0.93$  for both cases, these results predict  $E/E_o = 0.69$  at  $50 \text{ J}$  and  $0.39$  at  $12.5 \text{ J}$ , accounting for the observed drop in performance.

## Conclusions

Experimental tests on a cylindrically-symmetric Teflon electrothermal thruster have shown that the specific mass loss is linear with cavity length, and roughly independent of energy. The specific thrust is roughly constant with energy for high energies, but decreases for low energies. The highest specific impulse is achieved with the shortest cavity length.

Comparison with a two-stream model suggests that the fraction of late-time ablation is on the order of  $10\%$ , compared to  $40\%$  for the LES-8/9 thruster, and that a rarefaction wave model can be used to predict the impulse bit with an empirically-determined proportionality constant. Heat loss measurements as a function of discharge energy show a larger fraction of heat loss for lower energy, consistent with the observed reduced performance.

## Acknowledgements

We wish to acknowledge the enthusiastic support of J. Frus of Unison Industries, and valuable discussions with W. Solomon and D. Carroll of CU Aerospace, G. Spanjers and D. Bromaghim of the Air Force Research Laboratory, and I. Boyd and M. Keidar of the University of Michigan. We greatly appreciate the help and support of E. Antonsen of the Department of Aeronautical and Astronautical Engineering, and of D. King and J. Laystrom of CU Aerospace. We also thank M. Williams of the Department of Nuclear Engineering for his expert technical contributions, particularly in electronics, and K. Elam and D. Foley of the Department of Theoretical and Applied Mechanics machine shop for expert fabrication and short-notice support.

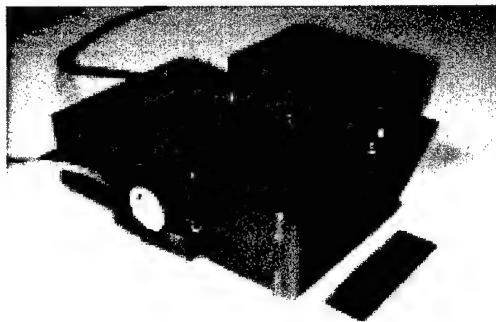


**Figure 1. PPT-7 Coaxial electrothermal pulsed plasma thruster.**

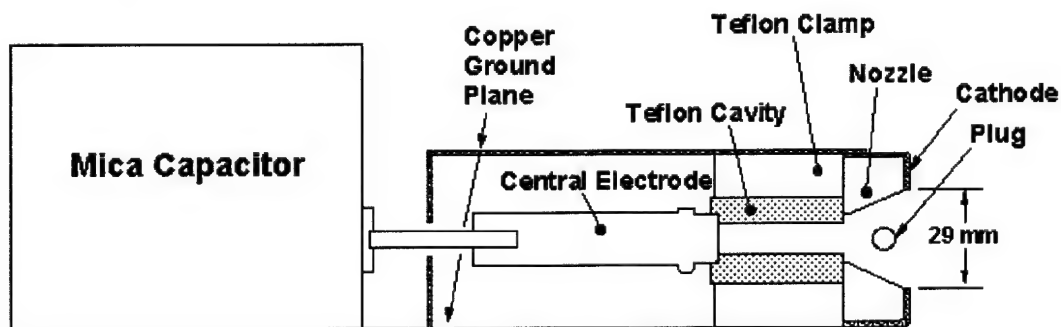


**Figure 2. Schematic of PPT-7**

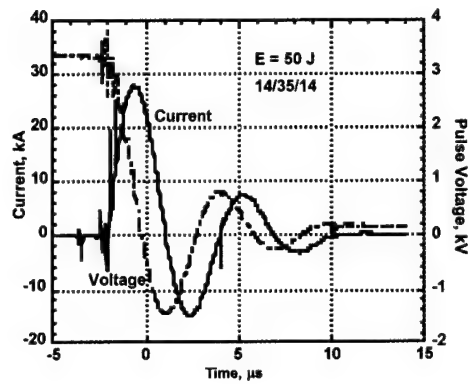


Figure 3. Baseline pulse current and voltage.

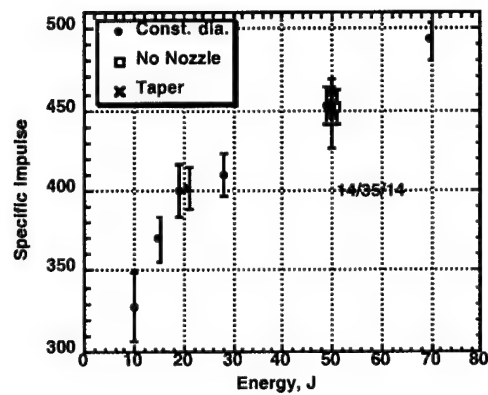


Figure 4. Specific impulse vs stored energy

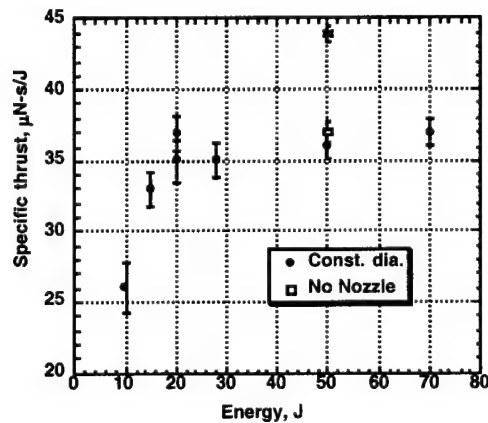


Figure 5. Specific thrust vs stored energy

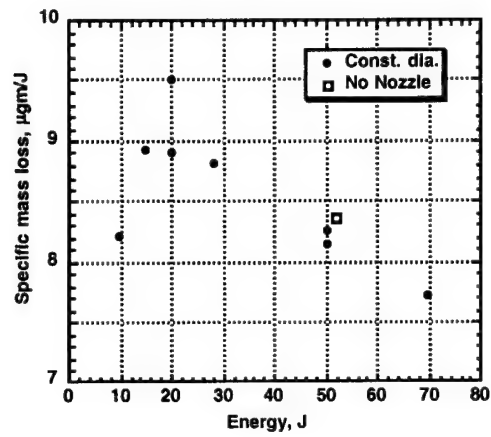


Figure 6. Specific mass loss vs stored energy

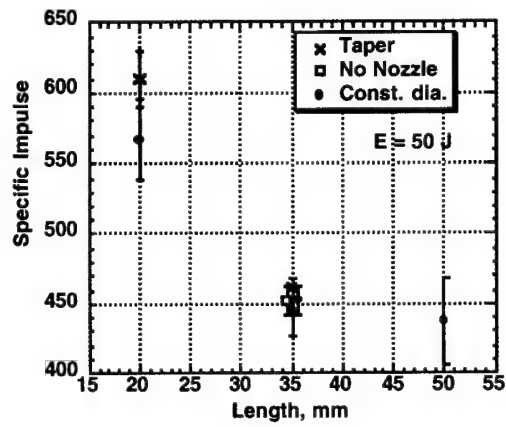


Figure 7. Specific impulse vs cavity length

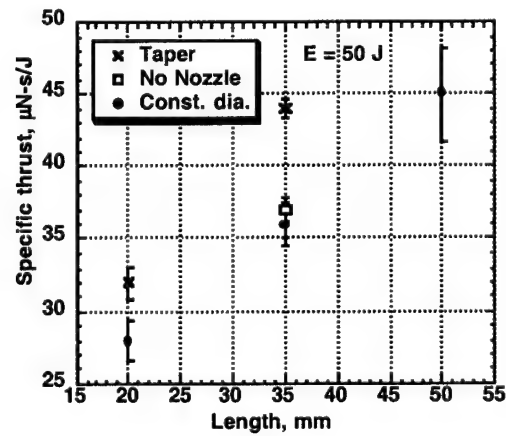


Figure 8. Specific thrust vs cavity length

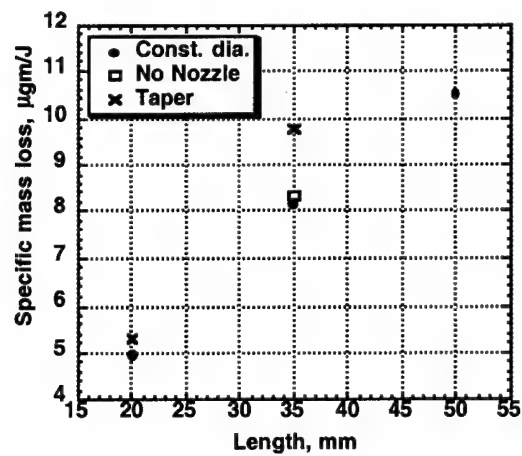


Figure 9. Specific mass loss vs cavity length

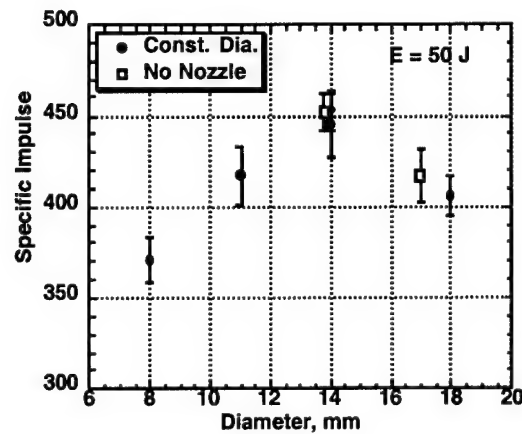


Figure 10. Specific impulse vs cavity diameter

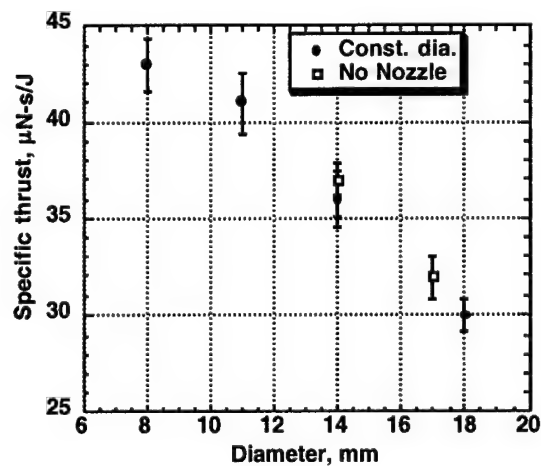


Figure 11. Specific thrust vs cavity diameter



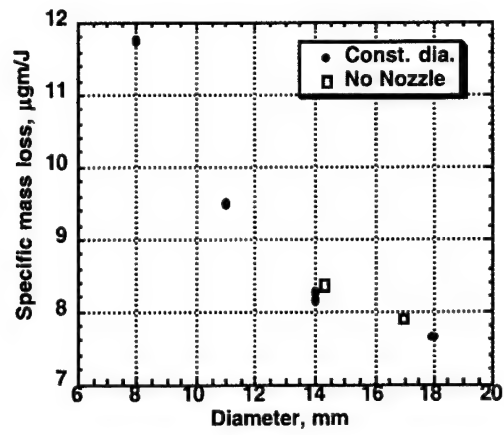


Figure 12. Specific mass loss vs cavity diameter

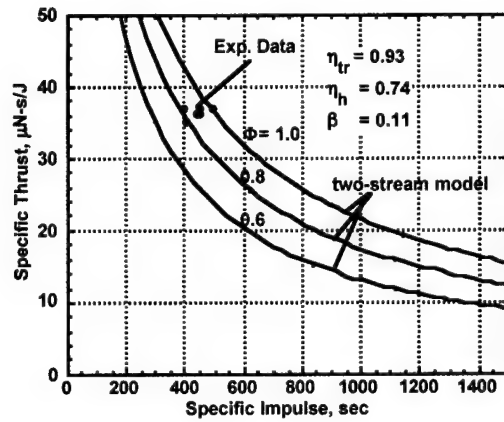


Figure 13. Comparison of experimental performance to two-stream model

## II. Diagnostics – Herriott Cell Interferometry

### Herriott Cell Interferometer for Unsteady Density Measurements in Small Length Scale Thruster Plasmas

The Herriott Cell Interferometer (HCI) augments state-of-the-art interferometry techniques with the path length multiplication afforded using the Herriott techniques. The result is an order of magnitude increase in resolution for density measurements. In addition, the various geometries attainable in the multi-pass beams enables the diagnostic to be optimized for diffuse, small-scale length plasmas. In its current implementation the diagnostic has been developed specifically for use on Pulsed Plasma Thrusters (PPTs).<sup>10</sup> The enhanced capability is needed to better understand the dynamics of the phase change from solid propellant to plasma accelerant. In addition, accurate measurements of the thruster exit plane density are required to develop models of spacecraft interaction from the use of PPTs in flight.

The attraction of the PPT as a propulsion option on small satellites stems largely from its design simplicity and use of solid, non-toxic propellant. However, in the past 30 years, research has failed to produce significant improvements in the overall performance of this thruster. Part of this is due to complex physics that are not completely understood. A typical efficiency for a state-of-the-art PPT is around 10%.<sup>11</sup> A critical source of the inefficiency is the poor use of propellant in the device. The PPT uses as little as 10% of its propellant to create thrust, the remaining 90% wasted in the form of small ionization fraction during the current pulse and late time vaporization after the pulse.<sup>10</sup> In order to improve this efficiency and harness the full potential of these thrusters, it is necessary to gain a more complete understanding of the physics behind their operation and of exactly how the propellant is being consumed.

As a further motivation for the diagnostic development, several near term flights have manifested, or are considering the use of PPTs.<sup>12</sup> A validated plume model can be valuable in optimizing the placement of the thruster on spacecraft so as to minimize possible interactions. Although models are in development for the PPT plume they lack the critical input conditions at the thruster exit plane, including electron and neutral densities. The increased sensitivity of the HCI enables these exit plane measurements.

Heterodyne quadrature interferometry has been used at the Air Force Research Laboratory (AFRL) to determine electron and neutral densities during single pulses of PPTs.<sup>19</sup> Unfortunately, at long timeframes random mechanical vibrations decrease the resolution below

that required to see the slow moving neutrals. In order to compensate for this effect, a Herriott cell was designed to increase the laser path length through the plasma through multiple passes.

The Herriott cell has been used for a variety of functions since its inception by D. Herriott for use as a laser resonator.<sup>13</sup> J. Altmann et al<sup>14</sup> first proposed its use in gaseous absorption measurements and it has been used extensively for that purpose. In addition, it has also been used for measurements of high reflectivity,<sup>14</sup> as an optical delay line,<sup>15</sup> and to produce a sequence of variable pulse separation light pulses.<sup>16</sup> The advantages of multiple passes in an interferometer are known but have been generally restricted to less than 5 passes attainable using flat mirrors. To the best of our knowledge this is the first use of a Herriott cell in an interferometric capacity where it is critical to maintain phase front integrity over a large number of reflections on a curved surface. Up to 18 passes have been demonstrated in the current effort. Measurement resolution increases linearly with the number of passes.

The Herriott cell also facilitates manipulation of the beam distribution within the plasma. With proper choice of mirror curvature and separation, the beams can be designed to converge on a single point, cover a plane, or partially fill a volume. The high accuracy single point measurement is especially attractive for small scale-length plasmas like that of the MicroPPT.<sup>17</sup> The planar measurement can be useful for characterizing the plasma flux through the thruster exit plane. The volumetric measurement can be used to measure the total plasma inventory within a thruster to characterize, for example, the conversion rate from solid Teflon to plasma.

## Herriott Cell Theory

A Herriott Cell consists of 2 concave mirrors facing each other in which laser light can be reflected a large number of times within the cavity. Often one of the mirrors has an off-axis admission aperture that allows entrance of the beam within the diameter of the mirrors themselves. Typically, the beam enters the cell through this aperture, reflects a number of times, and leaves the cell through the same aperture. The number of reflections is determined by the entrance conditions consisting of mirror separation, and entrance angles. The two mirrors facing each other can be adjusted in separation distance to increase the number of passes between them. In the general 3-dimensional configuration, the beam enters the cell at an angle offset both vertically and horizontally from the mirror centerlines and the reflection points trace an ellipse on the surface of each mirror. By eliminating the horizontal entrance angle the passes can be confined to a single vertical plane, ideal for measuring properties at the exit plane of rocket nozzles. Altmann<sup>17</sup> gives an analytic description for each bounce location during Herriott cell

operation along with exit slopes and total path length achieved within the cell. However, the bulk of the geometric cell analysis here was performed relying on 2 computer codes written specifically for optic raytracing analysis.

For the initial cell design, a ray-tracing code was written at Illinois with input parameters including mirror diameter, entrance angles, aperture location and size, mirror reflectivity, and mirror separation. Coupling the code output with the constraint that the mirror separation must be between the focal length and twice the focal length<sup>18</sup> of the two mirrors allowed a trade study that determined the initial design of the mirrors for the cell. The reason for this requirement stems from the fact that between the mirrors there is periodic focusing for multiple reflections caused by the mirror curvature. Separation distances outside this requirement do not allow the possibility of attaining an acceptable exit beam diameter without external focusing optics.

After the mirrors were designed and fabricated, computational analysis was performed using Beam3™ software<sup>19</sup> for the purpose of determining feasible testing geometries. The priority was to find a specific plane measurement mode that would cover the exit plane of the nozzle of a typical PPT. Using the Beam3™ code, a retro-reflection mode was discovered that allowed multiple pass numbers to increase with increasing separation and small-to-no variance in exit properties from the cell. This was one of the few geometries that allowed parallel or convergent exit beams from the cell.

Figure 14 shows 6 passes in the cell illustrated from the Beam3™ code. In this picture, the laser is entering from a 5 mm hole located in the upper half of the mirror on the left. The exit and entrance laser paths are co-aligned in this mode. By increasing the separation slightly, increasing numbers of passes can be achieved including 10, 14, 18, and 22 passes. Figure 15 and Figure 16 show 14 and 18-pass setups respectively. This retro-reflecting mode is achieved by sending the beam into the cell at 0° entrance angle both horizontally and vertically. Slight errors in entrance angle can be accommodated by adjusting the mirror tilt by small amounts. For this experiment, up to 18 passes were used, but in a practical sense, depending on the mirror diameter and the location of the entrance hole the number of passes is only limited by the reflectivity of the mirrors. The critical limit to the number of passes is that the output laser beam must be of sufficient intensity and phase front quality to perform interferometric analysis.

There was considerable interest in obtaining a point measurement technique that involved focusing the beams at the center of the cell for the purpose of future use in micro-propulsion diagnostics. This would allow convergence of all the beams at a single point, an ideal setup for measuring the density of small-scale length plasmas, such as the Micro-PPTs which have a diameter as small as 2 mm. The point measurement technique has been demonstrated in the

laboratory and modeled with Beam3™, but no data has been taken with it to date. Figure 17 shows the Beam3™ model of the point measurement geometry. The beam in Figure 17 is entering the cell from the top left, not through the aperture but over the side of the mirror. In addition, a lens is required to focus the incoming beam at the center of the cell equidistant from both mirrors, which are separated by a distance  $2R$ , where  $R$  is the radius of curvature of the mirrors. This configuration is more difficult to construct in a laboratory setup, requiring focusing both in to and out of the Herriott cell. When the optical alignment is optimized a single point of convergence for all beams is not truly achieved. There are 2 points of convergence very close to each other. By modifying the entrance angle and mirror tilt, the convergence point separation can be reduced to a few millimeters. This configuration can then be used experimentally in two possible modes. The first mode fires the microthruster horizontally across both convergence points causing a loss in spatial resolution of the plasma. The spatial resolution can be maintained using the second mode at a cost in instrument resolution. By firing the microthruster vertically through only one of the convergence points, a two-fold loss in instrument resolution is suffered while the spatial resolution is maintained.

### *Interferometry*

The interferometer is sensitive to several phenomena involved in the thruster operation. The phase change in the interferometer scene beam at the detector can be written as

$$\phi(t) = \phi_e(t) + \phi_n(t) + \phi_{PL}(t) \quad (1)$$

where the first term represents phase change due to the plasma electron density, the second term neutral density, and the third term physical changes in the path length difference between the two beams. In Eqn. (3) an index of refraction for the neutral Teflon exhaust has been estimated using the assumptions from Ref. 20. The phase shift due to the electron and neutral densities can be written (MKS-radians)<sup>20</sup>

$$\phi_e(t) = 2.8 \times 10^{-15} \lambda \int n_e dl \quad (2)$$

$$\phi_n(t) = \frac{3.9 \times 10^{-29}}{\lambda} \int n_n dl \quad (3)$$

where  $\lambda$  is the laser wavelength,  $n$  is the density, and the integral is performed over the path length through the probed region. The interferometer measures a line-averaged density, and requires suppositions concerning scale lengths and symmetry to reduce the measurement to a local density.

The final term in equation (1) is for changes in the path length which are dominated by vibrations physically moving optic components and air currents affecting local density and temperature gradients. This can be written as

$$\phi_{PL}(t) = \frac{2\pi\Delta l}{\lambda} \quad (4)$$

The  $\Delta l$  in the phase change for the path length difference represents the effective increase in optical path length for all of the environmental influences (vibration, air density, air temperature, and temperature gradients). The dominating effect here is the vibrational differences between the optics table where the laser and detection equipment are located and the in-tank optics table supporting the Herriott cell.

For this experiment, a single laser frequency is used. The data reduction scheme involves separating the PPT discharge into 2 domains dependent on the characteristics of the plasma at certain times. From time  $t_0 = 0 \mu s$  until after the PPT current pulse has ended (typically about  $20 \mu s$ ) the bulk of the phase shift is due to electron effects on the index of refraction. Since comparable amounts of neutrals have a negligible effect on the index of refraction the assumption is made that during the current discharge only electron density is being measured. During this phase, the contribution from physical path length changes is small due to the inherently low frequency of mechanical motion.

After the discharge has ended and there is no source of electrons or energy input (generally  $t > 20 \mu s$ ) the assumption is made that there is no contribution to changes in the index of refraction from electron density. The major contributors become neutral density and physical path length changes. Two frequencies can not be used to separate these two sources of phase shift since both have the same dependence on wavelength. In this case, the Herriott cell is especially valuable in increasing the sensitivity of the diagnostic to long-time-scale neutral density since the phase change due to neutral density increases linearly with the number of Herriott cell passes. The Herriott cell mirrors are rigidly fixed on an optic rail, and are not exposed to room air currents. Thus, it is expected (and shown experimentally) that the Herriott cell mirrors are not the dominant source of changes to the optical path length. The optic path between the optic table and the vacuum chamber always dominates. The phase change due to variations in the optic path length does not increase significantly with increased number of passes within the Herriott cell. This is shown in more detail below. Therefore, the accuracy of the neutral density measurement amidst environmental changes in the optic path length increases almost linearly with Herriott cell passes.

### *Phase Front Quality*

The main technical challenge to using the Herriott Cell for interferometric measurements is the ability to maintain a coherent phase front throughout the large number of reflections in the cell. The phase front is systematically distorted by imperfections in the optical surfaces from which it reflects. The high number of surface reflections will greatly decrease both the scene beam intensity and the quality of the phase front. Decreased intensity can be somewhat avoided by attenuating the intensity of the reference beam, or by adjusting the alignment of the acousto-optic modulator (Bragg cell) to increase the initial intensity of the scene beam. In practice, attenuating the reference beam by adding neutral density filters increases phase-front distortion. Adjusting

the Bragg cell is limited to a small range in intensity variation. In addition, quantitative measurements of the beam intensity are hampered by the very large beam diameters at the detector. These result from laser divergence over the long path lengths required with the Herriott cell.

The quality of the phase front is decreased during every interaction with an optical element. Even with high surface-quality mirrors in the Herriott cell, increasing the number of reflections will eventually distort the phase-front by full wavelengths across the beam diameter.

These effects can be examined analytically. At the detector, the electric field for the scene and reference beams can be written as

$$E_{\text{scene}} = E_s e^{i(\omega_A t + \phi(t) + \gamma(x,y))} \quad (5)$$

$$E_{\text{reference}} = E_R e^{i(\omega + \omega_A)t} \quad (6)$$

where  $\omega$  is the laser frequency,  $\omega_A$  is the acoustic frequency of the Bragg cell,  $\phi$  is the phase shift due to plasma and neutral density, and  $\gamma(x,y)$  represents a phase distortion across the beam diameter. The total electric field at the detector is the sum of these components. The output voltage of the detector is proportional to the intensity, which can be calculated from

$$V \propto I = \frac{1}{2} E E^* \quad (7)$$

where  $E$  is the sum of the scene and reference beams and  $E^*$  is the complex conjugate of that sum. After some algebraic manipulation this reduces to

$$V \propto \left( \frac{E_s}{E_R} \right)^2 \left[ 1 + \left( \frac{E_s}{E_R} \right)^2 + 2 \left( \frac{E_s}{E_R} \right) \cos(\omega_A t - \phi(t) - \gamma(x,y)) \right] \quad (8)$$

For  $E_R = E_s$  and perfect phase front ( $\gamma(x,y)=0$ ), this reduces to the familiar expression

$$V \propto 1 + \cos(\omega_A t + \phi(t)) \quad (9)$$

Note that the phase front distortion can be greatly minimized across the detector surface at the expense of intensity. It is standard operating procedure for the normal interferometer (no Herriott cell) to use a beam up to 5 mm in diameter that is detected with a 0.5 mm square photodetector. No focusing is used to direct the full beam intensity onto the detector. Instead, a small portion of the total beam is sampled. This has the predominant effect of increasing the spatial resolution from the diameter of the beam (5 mm) to the size of the photodetector active area (0.5 mm). Not focusing also reduces phase-front distortion, since the distortion has to occur over a scale length that is reduced by a factor of 10. For the interferometer with Herriott cell, the multiple reflections reduce the beam intensity, and the spatial resolution will be limited by the beam pattern within the cell. Therefore focusing may be used without significantly decreasing



the quality of the measurement. Multiple reflections also increase the likelihood that phase-front distortions could occur over the scale length of the photodetector active area.

Figure 18 shows Eqn. (8) plotted for several relative intensities of the scene and reference beams. As expected from Eqn (9), the "50-50" curve (equal intensity) shows a simple 40 MHz oscillation. As the intensity imbalance is increased, the 40 MHz signal remains, although its relative magnitude decreases. The signal also obtains a DC offset. This is equivalent to the loss of fringe contrast that occurs in the similar situation in 2-dimensional interferometers (without heterodyning). Band-pass filters at the input of the demodulation circuit will eliminate the DC offset leaving the 40 MHz signal with no phase distortion, albeit with a lower intensity. The reduced intensity will decrease signal-to-noise increasing random measurement uncertainty, but not introducing a more serious systematic uncertainty.

The effect of phase front distortion is examined using Eqn. (8) and assuming that the two beam intensities are equal. Functional forms for the  $\gamma(x,y)$  term are input, and the resultant voltage is calculated by integrating over the spatial extent of the recombined beam. A simple case of this analysis is illustrated in Figure 19 where the 40 MHz output waveform is calculated for various levels of phase-front distortion. The distortion here is assumed to be linear and only occur in one direction. Furthermore, the local intensities are integrated over a square cross-section indicative of the square active area of the photodetector. More detailed analysis (although still somewhat preliminary) shows similar results for cases where the phase distortion corresponds to that expected from reflection from a curved surface, and for the case of a circular cross section (appropriate when focusing is used). As the magnitude of the phase-front distortion increases, the intensity decreases, although the 40 MHz frequency remains. For 360-degree linear distortion, the 40 MHz signal disappears as expected. For distortion greater than a full wavelength, the 40 MHz signal reappears but with significant loss of intensity. Therefore significant phase-front distortion can be tolerated and still retain the 40 MHz acousto-optic frequency in the recombined beams. For curved phase fronts, similar effects are observed except that, (1) the 40 MHz signal can shift in phase as the phase-front distortion increases, and (2) at 360 degree average phase distortion, the 40 MHz signal may remain depending on the functional form assumed for the curvature.

The more critical issue is whether the phase-front distortion effects the apparent phase change that occurs when the plasma is introduced. We now show analytically by examination of Eqn. (8) that this issue is not a concern. This is examined in Figure 20 where two signals, one with no distortion and one with a distortion of 135 degrees, are each assumed to have a 60 degree plasma phase shift. Although the signal intensity is reduced, in the case with significant phase-front distortion the full 60-degree plasma shift is observed in the 40 MHz waveform at the detector. This indicates, for the linear distortion case, that the amount of phase shift caused by the plasma density is not changed through the process of integrating the intensity over the laser beam diameter of varying phases. Linear phase distortions do not cause systematic errors in the measurement of the plasma density. Analysis with curved phase fronts shows a similar conclusion of no systematic errors in the measurement.

## Experimental Apparatus

The PPT used for these measurements was the UIUC PPT-4, which is a co-axial, electrothermal PPT. The exit plane of the thruster is 4.44 cm in diameter. Fuel bars are side fed into a high pressure chamber and the exhaust is expanded out a boron nitride nozzle. The PPT performance was measured to have  $30 \mu\text{N}\cdot\text{s}/\text{J}$  and  $755 \text{ s } I_{sp}$ .<sup>21</sup> The PPT was supported above an optics table in the vacuum chamber and hung between the mirrors of the Herriott Cell. A small probe coil was placed between the capacitor terminals to trigger the scope used to obtain the firing data. Figure 21 shows the UIUC PPT-4 looking down the nozzle. The laser for the interferometer passes directly across the exit plane almost touching the brass front electrode. The PPT was fired at 20 J for each data point taken using four  $2 \mu\text{F}$  capacitors in parallel for a total of  $8 \mu\text{F}$ . There are diodes in parallel with the capacitors. Figure 22 shows the location of the PPT-4 exit plane within the beam spread provided by the 18 pass configuration. Figure 23 shows a schematic of PPT-4. The interferometer laser passes directly in front of the cathode.

The interferometer is laid out on a single optics table with the exception of the Herriott Cell that is stationed within the vacuum chamber. (Figure 24). Only the 488 nm wavelength laser was used, but transition to a 2-color system can be readily accomplished. The infrared laser can be added to allow separation of neutral and electron densities.

The beam exits the laser, passes through a 488 nm line filter, and a Bragg Cell which induces a 40 MHz oscillation acousto-optically. This splits the beam into the zeroth and first order beams which are taken as scene and reference beams respectively. The scene beam is then directed into the chamber and the Herriott Cell. Within the cell the scene beam reflects a pre-determined number of times and exits at a slight angle from the input beam allowing it to be picked off and recombined with the reference beam in a wavelength-tuned beamsplitter. From there the recombined beam goes into the photodetector. The scene and reference beams must have the same path length from the Bragg Cell to the recombining beamsplitter within a small percentage of the coherence length of the laser. For the Ar-ion laser used here, the coherence length was 10 cm, so the path lengths needed to be matched to within less than 1 mm. This was achieved using a micrometer mirror mount on an optical rail for the reference beam. The beam then entered and exited at a very small angle from the normal to the mirror surface. Rough tuning was done moving the mount manually and precise tuning then performed with the micrometer.

Following the recombination of the beams and measurement at the detector, the signal from the detector was then demodulated using a circuit consisting of 2 mixers, a power splitter, and a  $90^\circ$  phase shifter shown in Figure 25. The output of this circuit is the cosine and sine functions

of the unreduced phase shift. Reduction of the phase shift involves performing numerical quadrature on these signals through use of code written at AFRL.

### *Herriott Cell Design and Beam Shields*

The cell design included mirrors with a 2 inch diameter and a radius of curvature ( $r_c$ ) of 8 inches. Since  $r_c = 2f$ , the focal length was 4 inches for each mirror. On one mirror there is a 5 mm diameter admission aperture located 11 mm radially off the mirror axis. Smaller entrance holes were tested, but they reduced the intensity of the output light significantly. The location of the entrance hole is a constraint on the vertical spatial coverage that can be achieved with the Herriott Cell. Typically, the beam spread is contained within twice the off-axis diameter of the entrance hole. This can be stretched somewhat by using mirror tilting, but the effects are limited.

The mirrors used were  $\lambda/10$  surface flatness and coated with UV-enhanced aluminum coating. This coating has greater than 90% reflectivity from 250-600 nm, ideal for use of a 488 nm Argon ion laser and allows the possibility of using a 351 nm UV laser for greater neutral sensitivity offered by lower wavelengths. For a 633 nm HeNe laser, reflectivity is about 90% and for an IR laser at 1100 nm, reflectivity goes up to 92%. These colors can be used for greater electron density sensitivity in a two-color interferometer. Even at 90% reflectivity, only 15% of the light incident to the cell exits at 18 passes. This neglects aggravating effects from optics external to the cell. It is for this reason that more than 18 passes were not attempted. While the cell is capable of providing the required geometry, a higher power laser or higher reflectivity mirrors are required to make use of large numbers of passes.

The physical constraint limitation<sup>18</sup> of  $f \leq d \leq 2f$  defines the separation distance of the mirrors to between 4 to 8 inches for the retro-reflecting mode. This was initially thought to be adequate to allow for the nozzle of UIUC PPT-4 or the parallel plates of a LES 8/9 type PPT, but it was later determined that a larger mirror diameter (~3-4 in.) with a larger radius of curvature (~8 in.) is preferable. The necessity of a larger mirror diameter becomes apparent when attempting to measure a larger exhaust area. In this case, the off-axis location of the entrance hole becomes critical. For a 50.8 mm diameter mirror, placing the 5 mm diameter entrance hole at 21 mm off center will not provide a reflective beam pattern. The reason for this is that spot pattern on the mirror opposite the beam entrance is slightly larger than the entrance hole distance from the mirror axis. In addition, a larger radius of curvature is of interest because it allows a greater mirror separation for the same number of passes. At first glance, this would appear to be counterproductive owing to greater beam dispersion over an already extensive total path length. Unfortunately, PPT exhaust impacting mirrors aggravates mechanical vibrations already present

increasing the amplitudes by significant fractions of a phase shift, thereby masking late-time neutral densities. This conclusion was reached through a series of tests. The increased vibrations were witnessed at late times when the PPT was fired between the mirrors. Covering the PPT with a plastic bag did not produce the same vibrations and ruled out the possibility of mechanical vibrations from the PPT shaking. The PPT was then placed outside the mirrors such that the exhaust could impact the back of one of the mirrors. The mechanical vibrations returned. Figure 26 shows this effect on a long timeframe compared to the natural mechanical vibrations. This effect dramatically increased the uncertainty in measurements collected after 300  $\mu$ s making impossible to witness the return of measured neutral density to zero. Diagnostic improvements aimed at preventing or delaying the exhaust impingement on the mirrors may be effective in enabling neutral density measurements beyond the 300  $\mu$ s time.

Initially, concerns about exhaust-mirror interactions were geared toward the buildup of Teflon on the mirrors and the effects of these coatings on reflectivity. Beam shields were therefore designed to minimize the exposed surface area by providing a metal cover over the mirror with a slot allowing vertical reflections. Figure 27 shows the Herriott cell with beam shields in place. The beam shields failed to damp the amplified mechanical vibrations attributed to exhaust impact. They had no noticeable effect on the measurements taken.

## Experimental Results

### *Density vs. Number of Passes*

Tests were conducted using PPT-4 under the same testing conditions for various numbers of cell passes. From 2 to 18 passes were tested to compare the measured densities and determine statistical and systematic uncertainties. The 2-pass system was simply a flat mirror returning the beam through the plasma. Six, 14 and 18 pass tests were performed for comparison to the 2-pass setup. In comparing data from these four methods detailed attention must be paid to the uncertainty analysis. In 2-pass setup, the largest source of uncertainty is the mechanical vibrations introduced between the mirrors in the vacuum chamber and the optics table with the laser and photodetectors. When an additional Herriott cell mirror is added in the tank, some increase in vibrational uncertainty is expected. For the Herriott Cell to be effective, the increase in vibration-induced phase shift must be small compared to the increase in density-induced phase shift, as additional laser passes are added between the Herriott cell mirrors. In this case, the vibrational noise level remains constant while the resolution of the instrument is increased proportional to the number of passes. In addition to that requirement, different numbers of

passes should return the same electron and neutral densities within the shot-to-shot variation of the thruster being tested since there is no systematic error introduced by the Herriott Cell. Figure 28 shows the increase in phase shift for increasing number of passes in the cell for both the neutral density signal due to a single data shot along with the mechanical noise induced mainly by mechanical vibrations. These data were taken at 200  $\mu$ s into the pulse and as such are due only to neutral density and mechanical noise. The 4 solid data points are shots taken from different data sets on PPT 4 and are not an average, each represents a single measurement. As such the uncertainty is the noise signal represented by the hollow data points. The data points are the phase shift data for each shot shown. At 200  $\mu$ s into the pulse, the vibrational uncertainty is approximately  $\pm 19^\circ$  for each different number of passes in the Herriott Cell. For the case of the 2-pass interferometer, the uncertainty is  $\pm 10^\circ$ . From 2 – 6 passes, there is an increase in the vibrational uncertainty that corresponds to the addition of the extra optic for the Herriott Cell. Thus going from a single pass interferometer to a Herriott cell arrangement decreases the resolution by half due to the increased vibration of adding the second Herriott cell mirror. However, the increase to 18 passes within the Herriott cell results in an 18-fold increase in measurement sensitivity. In addition, the  $19^\circ$  uncertainty measured for the Herriott Cell system is only a consequence of the vibration suppression measures taken and can vary from system to system. In favorable conditions, the vibrational uncertainty at long timeframes can become significantly lower.

#### *Uncertainty Terms*

The increase in phase shift measured for a given thruster is linear with an increase in passes within the shot-to-shot variation of the thruster itself. In the case of a PPT, the uncertainty in density is expressed as

$$\Delta n = \sqrt{\Delta n_{\text{vib}}^2 + \Delta n_{\text{PPT}}^2} \quad (10)$$

where  $\Delta n_{\text{vib}}$  is the uncertainty due to vibrations and  $\Delta n_{\text{PPT}}$  is the shot-to-shot variation of the PPT. The vibrational uncertainty is quantified as

$$\Delta n_{\text{vib}} = C \frac{\Delta \phi}{N} \quad (11)$$

where  $N$  is the number of passes through the plasma. For increasing numbers of passes the Herriott cell serves to reduce vibrational uncertainty at long timeframes. The firing deviation for electron density peaks is  $\pm 50^\circ$  due mainly to the shot-to-shot envelope ( $\Delta n_{\text{PPT}}$ ) of the thruster itself while the vibrational deviations are only  $\pm 0.5^\circ$ . Therefore the Herriott Cell offers no advantage early in the pulse. The number of passes has no effect on the  $\Delta n_{\text{PPT}}$  term in equation (10), which is dependent on the firing repeatability of the plasma source being measured.

Although there is no direct dependence on phase shift for the statistical term, at late times it is possible for the vibrational uncertainty to overwhelm the statistical variation observed.

Figure 29 shows 2 pass data at 200  $\mu\text{s}$  into the pulse. The top trace is mechanical vibrations measured by taking data when no thruster was firing. It is an average of 20 shots per data point. These data are converted to the neutral density that the produced phase shift would be interpreted as if the thruster were firing. The error bars are the standard deviation of those data shots. The bottom trace is data taken when the thruster is firing. The phase shift contribution here is due to both neutral density and mechanical vibrations. It is apparent that the neutral density here is swamped by the mechanical vibrational contribution. Without the increase in resolution from the Herriott cells, the standard interferometer fails to produce a definitive neutral measurement.

Figure 30 shows a single set of data for 18 passes. The measured mechanical vibrations and the uncertainty they introduce are plotted along with that data showing the distinct measurement of neutral density with the increased resolution of the Herriott cell. In this case special attention is paid to the timeframe between 20 and 180  $\mu\text{s}$ . During this timeframe, the average firing data from the 20 shots recorded lies outside the negative standard deviation for the vibration measurements. This is an indication of neutral density measurement with 18 passes in the Herriott cell. This data set shows a measured neutral density of  $3 \times 10^{15} \text{ cm}^{-3}$  increasing almost linearly to  $7 \times 10^{15} \text{ cm}^{-3}$  from 20 to 200  $\mu\text{s}$  after the pulse. Around 200  $\mu\text{s}$  the vibrational noise begins to mask the measured neutral data.

## Discussion of Results

There are two important limitations in this measurement. First, for times less than 20  $\mu\text{s}$ , the electron density causes large phase shifts in the opposite direction to that of the neutrals. Within this measurement, large neutral densities are possible, however, the measurement technique is several orders of magnitude more sensitive to electron densities, so that high neutral densities at early times are completely masked by the electron densities. In order to resolve this, a second laser frequency must be added to the interferometer.

Second, after 200  $\mu\text{s}$  the recorded data for 18 passes falls within the uncertainty created by mechanical vibrations. This is not indicative of the neutral density returning to zero but only shows that at late times the uncertainty increases to the point of masking the neutral density. We now use the neutral density to compare to the known PPT-4 mass ablation.

The neutral density data in Figure 30 can be approximated as linear from 20 to 200  $\mu\text{s}$ . The velocity of these cool particles is estimated as  $v \sim 300 \text{ m/s}$  allowing an estimate of the total mass represented by the neutral density measurement from 20 to 200  $\mu\text{s}$  as  $\Delta m = \int_{20 \mu\text{s}}^{200 \mu\text{s}} m_n n_n A v dt$ . The exit area  $A$  is  $0.0015 \text{ m}^2$  and the average Teflon particle mass is  $15.5 \text{ g/mol}$ . From this calculation, the mass of the slow neutrals per pulse corresponding to the measured neutral density is  $10 \mu\text{g}$ , compared to about  $80 \mu\text{g}$  for PPT-4 at 20 J.

An estimation of the contribution of each type of thrust mechanism active in PPT-4 can be performed.

Table 5 shows a breakdown of the contributing thrust mechanisms, where the total impulse bit has been measured [Ref 21], and the electro-magnetic  $I_{bit}$  is calculated for uniform current density. The late-time ablation contribution is  $\Delta m v$ .



Table 5. Breakdown of Thrust Contributions

Thrust Source	$I_{bit}$ ( $\mu\text{N}\cdot\text{s}$ )	% $I_{bit}$
Total	600	100
Electrothermal	515	86
Electromagnetic	82	13.5
Late-Time	3	0.5
Ablation		

These results agree with PPT-4 results,<sup>21</sup> indicating that the neutral density measurement is roughly correct. PPT-4 emits about 80  $\mu\text{g}$  per pulse at 20 J, so that the late-time ablation is estimated as 15% during the 20-200  $\mu\text{s}$  window, a not unreasonable number. However, because the measurement technique is limited at late times by increasing vibration uncertainty, it is possible that more mass is ablated for  $t > 200 \mu\text{s}$ .

For PPTs, the measured densities are variable within a statistically determined range. For this reason, both electron and neutral densities are averaged over a large number of shots with statistical error bars demonstrating the range of the performance variation from shot to shot. The standard deviation at any specific time over large sampling of firings determines the uncertainty  $\Delta n_{\text{PPT}}$ . Depending on what time during the pulse is of interest, either of these uncertainties can be dominant. Figure 31 shows the electron density at time 4  $\mu\text{s}$  after the pulse. This measurement is an average of all data sets for a particular number of passes. Measured electron density showed peak density at 4  $\mu\text{s}$  to be  $5.0 \pm 1.1 \times 10^{15} \text{ cm}^{-3}$ . The vibrational uncertainty bars here are smaller than the data point used to represent each point because they correspond to  $\pm 0.5^\circ$  early in the pulse. The dominant uncertainty at this point is clearly the shot-to-shot variation of the thruster itself. It is clear that the Herriott Cell is not necessary to make electron density measurements, within the assumption of neglecting any neutral density contribution during the discharge pulse. For varying numbers of passes, the measured electron densities fall within the statistical uncertainty bars of each other. This experimentally verifies the above analytical conclusion that there is no systematic error induced by the Herriott Cell.

The case of the neutral densities is different because the measurement occurs later in the pulse. Vibrational uncertainty can be comparable to the statistical differences in thruster firings in this regime. Figure 32 shows the neutral densities at 200  $\mu\text{s}$  into the pulse, showing the neutral density at 200  $\mu\text{s}$  to be no more than  $1 \times 10^{16} \text{ cm}^{-3}$ . These data points are an average over all sets of data for each different number of passes. The 2-pass data is representative of 2 data sets or 40 measurements. For the 6-18 pass cases, each point is representative of 60-120 data points. The benefits of many passes are demonstrated in the decreasing size of the error bars at late times. Both the vibrational and total uncertainties are decreasing as a function of the number of passes in the Herriott Cell. At this point the vibrational uncertainty dominates allowing total uncertainty to decrease significantly as a function of passes.

## Conclusions

The Herriott cell can be a valuable addition to interferometry for use in determining neutral densities and density measurements of small-scale length plasmas and gas flows. Experimental and analytical analysis demonstrates that the integrity of the phase front is retained at a quality high enough for interferometric purposes. Comparison of a 2-pass setup with varying numbers of passes in the Herriott cell was performed. Over varying number of passes in the cell the electron and neutral densities measured consistently fell within the statistical shot-to-shot variation of the thruster used. At early times in the pulse, the statistical variation of the thruster itself dominates the uncertainty term. Later in the pulse physical path length changes due to external vibration sources come to dominate the uncertainty of the measurement. In this regime the Herriott cell becomes invaluable to the operation of the diagnostic. Application to small-scale plasmas generated by pulsed micro-thrusters is yet to be tested, but the required geometries have been demonstrated in the laboratory.

## Acknowledgements

This work was funded by the Air Force Office of Scientific Research, under Contract No. F49620-98-1-0123 in support of TechSat 21. M. Birkan is the Program Monitor

## Figures

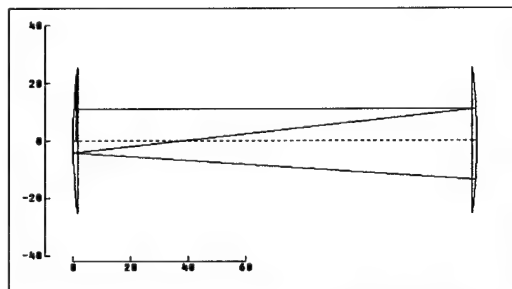


**Figure 14. Herriott cell with 6 passes in retro reflecting mode plotted using Beam3™.**  
Units are in mm.

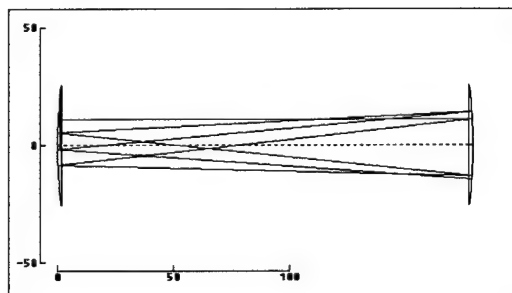


**Figure 15. 14 passes in retro-reflecting mode. Units in mm.**

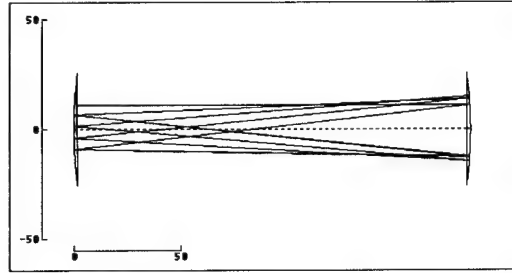


**Figure 16. 18 passes in retro-reflecting mode. Units in mm.**

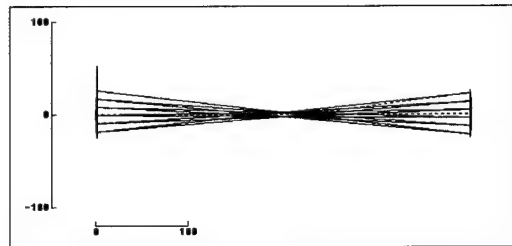


**Figure 17. Herriott cell in the Point Measurement Geometry. Beam enters above the left mirror. Units in mm.**

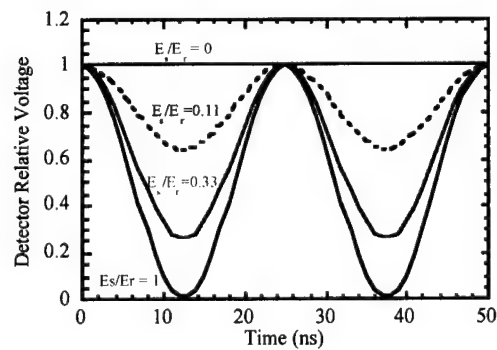


**Figure 18. Effect of non-balanced intensities on the interferometer signal at the detector. Relative intensities of the scene and reference beams are given above each trace.**

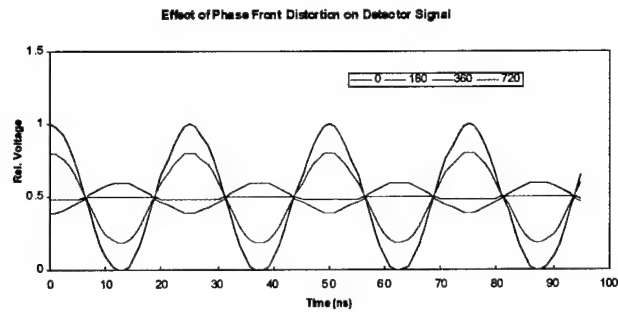


**Figure 19. Detector output signal for varying magnitudes of phase-front distortion. The trace labeled “0” corresponds to zero phase distortion, “180” corresponds to  $\lambda/2$  wavelength distortion, etc. In each case, the distortion is presumed linear in one direction across the beam diameter and the beam is presumed square.**

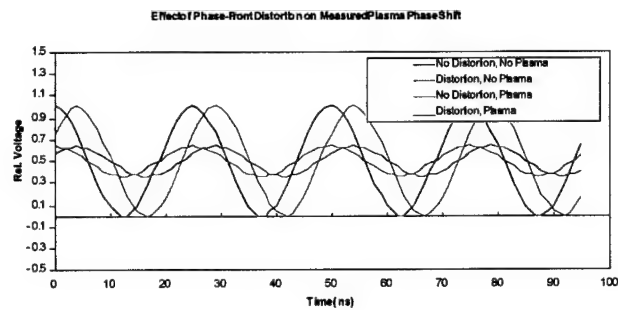


**Figure 20. Effect of Phase-front distortion when a plasma-induced phase shift is present.**

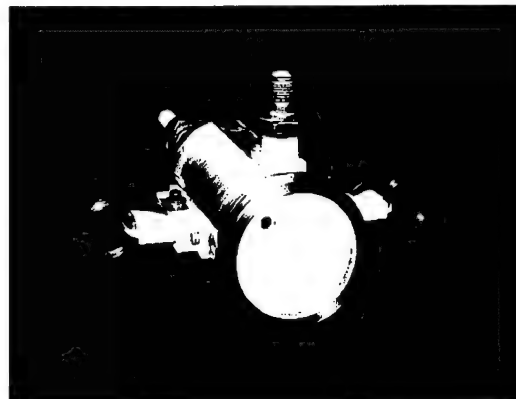


**Figure 21. Frontal View of UIUC PPT-4.**

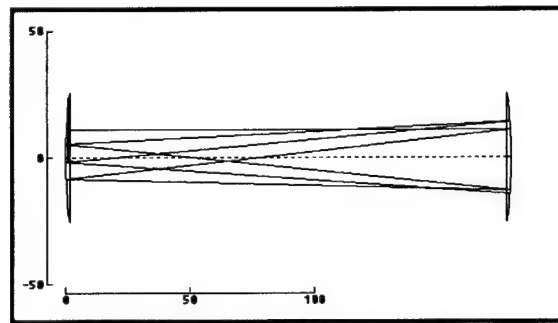


Figure 22. 18 pass configuration showing location of PPT-4 exit plane (mm).

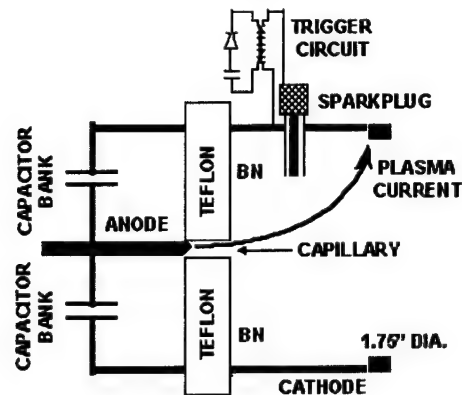


Figure 23. Schematic of PPT-4.

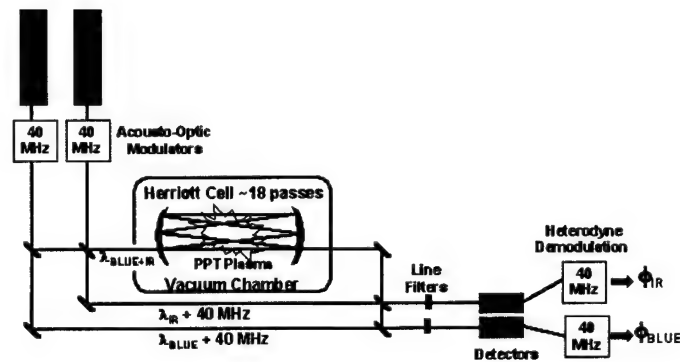
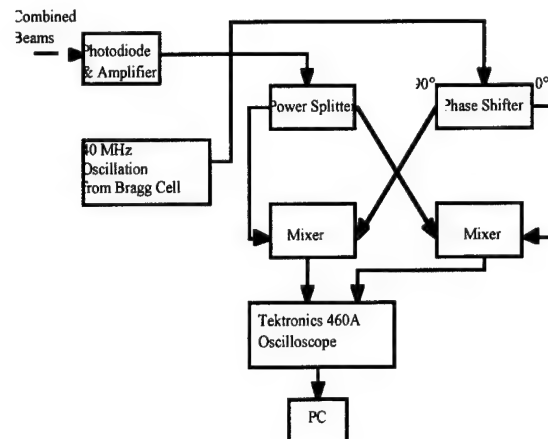
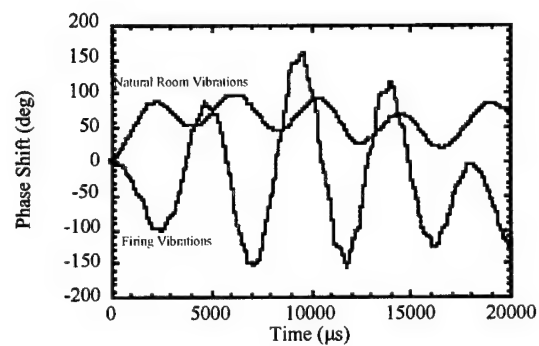


Figure 24. Interferometer layout with optional second wavelength.



**Figure 25. Post detection processing schematic.**



**Figure 26. Plasma-mirror interactions increase mechanical vibration amplitudes.**

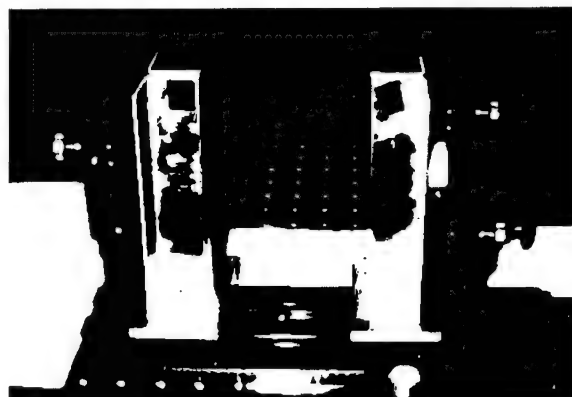


**Figure 27. Herriott Cell with Beam Shields.**

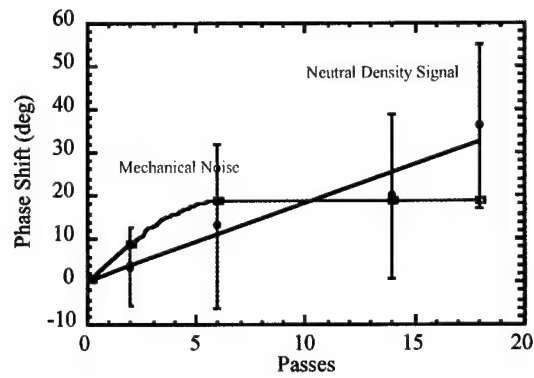


**Figure 28. Mechanical noise plotted with 4 single data shots at 200  $\mu\text{s}$  after the pulse shows the increase of measurement resolution beyond the uncertainty due to mechanical vibrations.**

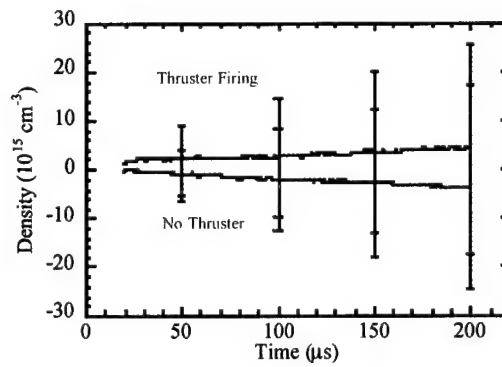


**Figure 29. A 2-pass data set showing mechanical vibrations and neutral measurements. Here the neutral data is swamped by vibrational uncertainty.**



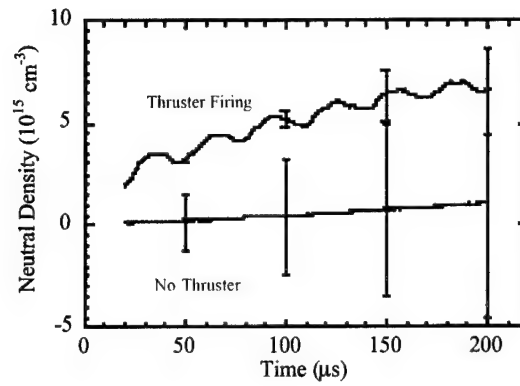


**Figure 30. An 18-pass data set showing mechanical vibrations and neutral density. The resolution is adequate to distinctly separate neutral density.**

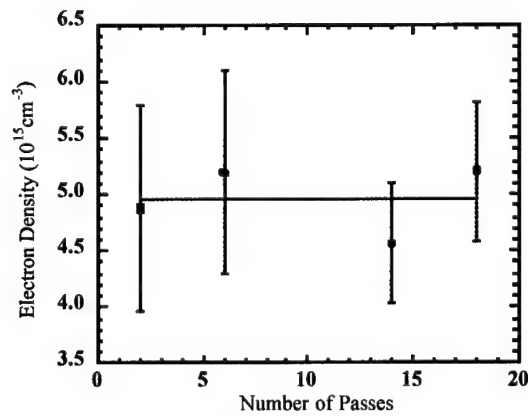


**Figure 31. Electron densities at 4 μs for increasing number of passes with statistical and vibrational uncertainty bars. The vibrational uncertainty error bars are smaller than the data points.**

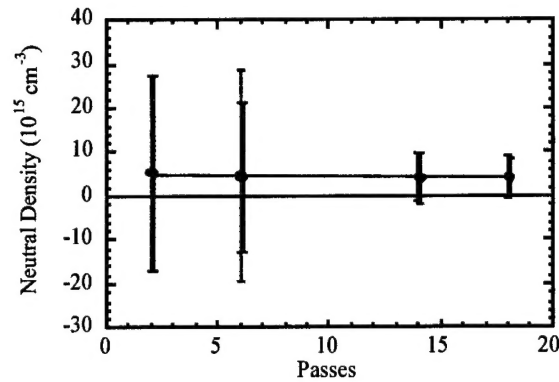


**Figure 32. Neutral densities at 200 us for increasing number of passes with statistical and vibrational uncertainty bars.**

### III. Modeling -- Two-Stream Model

Under this contract we have developed a new theory of PPT operation called the Two-Stream Model, which has led to increased understanding of PPT operation, greatly increased performance, and shows the way to a new class of high- $I_{sp}$  PPTs with much higher efficiency.

Previous spectroscopic velocity measurements in the PPT plume gave velocity data, as shown below. The important point is that the ion ( $C^+$ ,  $F^+$ ) speed is faster than the neutral ( $C$ ,  $N$ ) speed by about 10 - 15 km/s.

#### **Measured Particle Velocity**

Particle	u (km/s)
C	3 - 10
F	3 - 10
$C^+$	20 - 30
$F^+$	15 - 20

In the Two-Stream model<sup>22</sup>, the thruster efficiency is written as the product of sub-system efficiencies:

$$\eta_t = \eta_{tr} \times (1 - \eta_\ell) \times \eta_f \times \eta_{div} \times \eta_{dist}$$

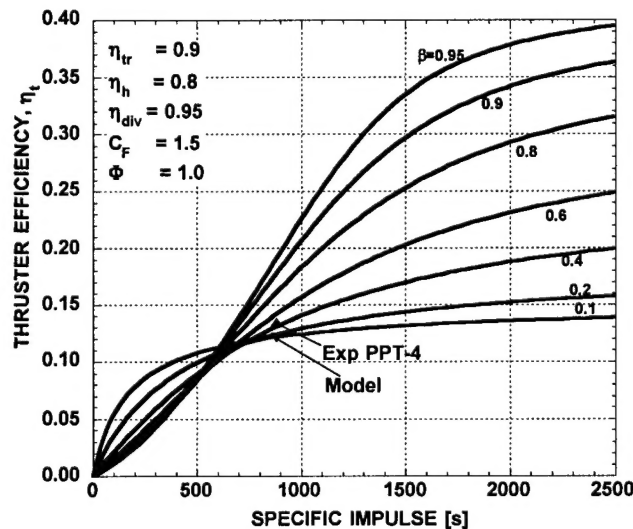
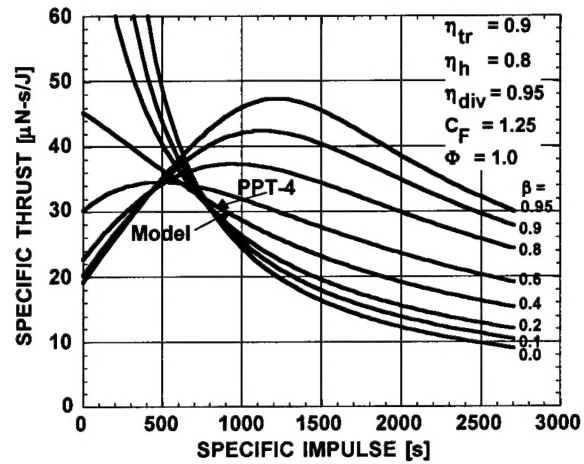
corresponding to energy transfer (tr) from capacitor to arc discharge, heat loss ( $\ell$ ) to the wall, frozen flow loss (f) in the exhaust, off-axis exhaust beam divergence (div), and loss due to the velocity distribution difference (dist) of fast and slow exhaust particles.

The theory assumes that the exhaust stream is split into two co-flowing streams, one fast and one slow, which average together to give the measured thrust and specific impulse. A key hypothesis, justified from the work of Alfven and related experiments on partially ionized plasmas [refs. available], is that the velocity difference of the two streams is equal to the Alfven critical velocity:

$$u_{\text{fast}} - u_{\text{slow}} = u_c = \sqrt{2eV_i / m} = 13.3 \text{ km/s}$$

where  $V_i$  is the ionization potential. This hypothesis is in approximate agreement with the velocity data in the table above. A second key hypothesis is that the electromagnetic thrust fraction  $\beta$  accelerates the fast particles and the remaining electrothermal thrust  $(1 - \beta)$  accelerates the slow particles. Empirical factors in the theory are the nozzle thrust factor  $C_F$  and the late-time ablation factor  $\Phi$ . Using empirical data for the thruster losses gives the theoretical specific thrust and specific impulse as shown in the two figures below:

This theory predicts the performance of the PPT over a wide operational range, as seen in the graphs above for a coaxial thruster. The theory predicts two major trends. A regime exists below 800 seconds  $I_{sp}$  where electrothermal PPTs have very high thrust, 2-3 times the usual value of 15  $\mu\text{N-s/J}$ . This region is being exploited for TechSat21, as shown in the PPT-4 data. A second regime exists for electromagnetic PPTs ( $\beta > 0.8$ ) where both high thrust and high  $I_{sp}$  (>2500) sec can be achieved, resulting in efficiencies approaching 40%.



## References

1. R. L. Burton, P. J. Turchi, "Pulsed Plasma Thruster," *Journal of Propulsion and Power*, Vol. 14, No. 5, 1998, pp. 716-735.
2. Unison Industries, Jacksonville, FL 32256
3. Wilson, M. J., Bushman, S. S., and Burton, R. L., "A Compact Thrust Stand for Pulsed Plasma Thrusters," IEPC Paper No. 97-122, 25th International Electric Propulsion Conference, Cleveland, OH, Aug., 1997.
4. Bushman, S. S., Burton, R. L., and Antonsen, E. L., "Arc Measurements and Performance Characteristics of a Coaxial Pulsed Plasma Thruster," AIAA Paper No. 98-3660, July, 1998.
5. Bushman, S. S., "Investigations of a Coaxial Pulsed Plasma Thruster," University of Illinois M.S. Thesis, University of Illinois College of Engineering Rpt. No. UILU-ENG 99-0509, AAE Report 99-09, 1999.
6. Keidar, M., "Electrical Discharge in the Teflon Cavity of a Coaxial Pulsed Plasma Thruster," IEEE Transactions on Plasma Science, Vol. 28, No. 2, Apr. 2000.
7. Burton, R. L., Rysanek, F., Antonsen, E. A., Wilson, M. J., and Bushman, S. S., "Pulsed Plasma Thruster Performance for Microspacecraft Propulsion," Chap. 13, AIAA Progress Series, Micropropulsion for Small Spacecraft, M. Micci, ed., 2000.
8. Spitzer, L., Physics of Fully Ionized Gases, 2nd Ed., Interscience Publishers, 1962.
9. Kovitya, P., "Thermodynamic and Transport Properties of Ablated Vapors of PTFE, Alumina, Perspex, and PVC in the Temperature Range 5000 - 30,000 K," IEEE Transactions on Plasma Science, Vol. PS-12, No. 1, March 1984, pp 38 - 42.
10. R. L. Burton, P. J. Turchi, "Pulsed Plasma Thruster," *Journal of Propulsion and Power*, Vol. 14, No. 5, 1998, pp. 716-735.
11. G. G. Spanjers, J. B. Malak, R. J. Leiweke, R. A. Spores, "The Effect of Propellant Temperature on Efficiency in a Pulsed Plasma Thruster," AIAA Paper No. 97-2920, July 1997.
12. D. R. Bromaghim, G. G. Spanjers, R. A. Spores, R. L. Burton, D. Carroll, J. H. Schilling, "A Proposed On-Orbit Demonstration of an Advanced Pulsed-Plasma Thruster for Small Satellite Applications," Proceedings of the 2000 IEEE Aerospace Conference, March 2000.
13. D. R. Herriott, H. Kogelnik, R. Kompfner, "Off- Axis Paths in Spherical Mirror Interferometers," *Applied Optics* 3, 1964, 523.

14. J. Altmann, P. Pokrowsky, "Sulfur Dioxide Absorption at DF Laser Wavelengths," *Applied Optics* Vol. 19, No. 20, 1980, pp. 3449-3452.
15. D. R. Herriott, H. J. Schulte, "Folded Optical Delay Lines," *Applied Optics* Vol. 4, No. 8, 1965, pp. 883-889.
16. J. Brochard, P. Cahuzac, "Use of Multi-Path Optical Cavities in some Saturated Absorption Experiments. Frequency Scale and Optical Delay Line." *J. Optics (Paris)* Vol. 8, No. 3, 1977, pp. 207-211.
17. R. A. Spores, M. Birkan, "The Air Force Electric Propulsion Program," AIAA Paper No. 99-2706, CA, June 1999.
18. J. Altmann, R. Baumgart, C. Weitkamp, "Two Mirror Multipass Absorption Cell," *Applied Optics* Vol. 20, No. 6, 1981, pp. 995-999.
19. Stellar Software, Berkeley, CA, [www.stellarsoftware.com](http://www.stellarsoftware.com)
20. G. G. Spanjers, K. A. McFall, F. S. Gulczinski, R. A. Spores, "Investigation of Propellant Inefficiencies in a Pulsed Plasma Thruster," AIAA Paper No. 96-2723, July 1996.
21. S. S. Bushman, *Investigations of a Coaxial Pulsed Plasma Thruster*, MS Thesis, University of Illinois at Urbana-Champaign, 1999.
22. Burton, R. L., Rysanek, F., Antonsen, E. A., Wilson, M. J., and Bushman, S. S., "Pulsed Plasma Thruster Performance for Microspacecraft Propulsion," AIAA Progress Series in Astronautics and Aeronautics, M. M. Micci and A. D. Ketsdever, eds., Ch. 13, pp. 337-352, 2000